arXiv:1301.0754v1 [physics.comp-ph] 4 Jan 2013

A simulation method for determining the optical response of highly complex photonic structures of biological origin

A.E. Dolinko[a,b], D.C. Skigin[a]

[a] *Grupo de Electromagnetismo Aplicado, Departamento de Fisica, FCEN, Universidad de Buenos Aires, and IFIBA - CONICET, Ciudad Universitaria, Pabellon I, C1428EHA Buenos Aires, Argentina.*

[b] *Departamento de Biodiversidad y Biología Experimental, Facultad de Ciencias Exactas y Naturales, Universidad de Buenos Aires, Ciudad Universitaria, Pabellón II, C1428EHA Buenos Aires, Argentina.*

Abstract

We present a method based on a time domain simulation of wave propagation that allows studying the optical response of a broad range of dielectric photonic structures. This method is particularly suitable for dealing with complex biological structures. One of the main features of the proposed approach is the simple and intuitive way of defining the setup and the photonic structure to be simulated, which can be done by feeding the simulation with a digital image of the structure. We also develop a set of techniques to process the behavior of the evolving waves within the simulation. These techniques include a *direction filter*, that permits decoupling of waves travelling simultaneously in different directions, a *dynamic differential absorber*, to cancel the waves reflected at the edges of the simulation space, a multi-frequency excitation scheme based on a filter that allows decoupling waves of different wavelengths travelling simultaneously, and a near-to-far-field approach to evaluate the resulting wavefield outside the simulation domain. We validate the code and, as an example, apply it to the complex structure found in a microorganism called *Diachea leucopoda*, which exhibits a multicolor iridescent appearance.

Keywords: photonic simulation; complex nanostructures;structural color;

Email address: adolinko@df.uba.ar (A.E. Dolinko)

nanobiology.

1. Introduction

The study of the optical response of structures with typical sizes of the order of the optical wavelengths has gain great interest in recent years. Emerging technologies had resulted from the study of photonic materials, which consist of a regular distribution of particles within a host matrix. Depending on the size of the inclusions relative to the operating wavelength, photonic materials can be classified in metamaterials (characteristic size significantly smaller than the wavelength) and photonic crystals (characteristic size of the order of the wavelength). Then, metamaterials operating within the visible range are nano-structured dielectric or metallic materials, which are designed to control the effective electric permittivity and magnetic permeability in order to obtain a specific response. In particular, the possibility of generating a material with negative refraction index [1] led to a great variety of promising applications, such as superlensing and optical cloaking [2, 3, 4, 5, 6]. On the other hand, all-dielectric photonic crystals exhibit interesting properties that arise from the resonant scattering generated by the specific modulation of the refraction index in a dielectric transparent material [7, 8, 9]. Photons in this kind of medium play the same role as electrons in the atomic crystal lattice [10, 11], and then the photonic system also exhibits band gaps, i.e., forbidden bands for the propagation of waves. These artificial materials can be designed for specific purposes such as optical switches, Bragg filters or photonic crystal fibers [12, 13, 14].

Another growing research field based on dielectric photonic structures is the study of natural structural color, which is responsible for the iridescent appearance that exhibit a broad diversity of animals and plants [15, 16, 17]. Structural color is produced by the selective reflection of light incident on the microscopic structures present in the cover tissues of biological organisms. Optical mechanisms such as interference, diffraction and scattering are involved to achieve colorful patterns or metallic appearance. These colors usually appear considerably brighter than those of pigments, although they often result from completely transparent materials [18, 19]. Unlike artificial photonic materials, the geometry and distribution of these natural media is usually extremely complex, and the simulation of their electromagnetic response require versatile and accurate tools. The study of this phenomenon

contributes to understand different behavioural functions of living species such as thermoregulation and camouflage and, at the same time, inspires new developments of artificial devices.

A large variety of rigorous electromagnetic methods to obtain the optical response of a given photonic structure are available in the literature. Among these methods, we can mention the modal method [20, 21, 22, 23, 24], coordinate-transformation methods [25, 26] and the integral method [27, 28, 29]. These approaches are very efficient for the accurate determination of the optical response of corrugated interfaces and periodic gratings of canonical shapes. However, in most cases this kind of methods are not suitable for dealing with highly complex structures.

Another way of studying the electromagnetic response of complex nanostructures is by means of computer simulations. A very spread approach is the *Finite Difference Time Domain* method (FDTD) introduced by Taflove *et al.* around 40 years ago [30]. This method is based on the Yee algorithm [31] and consists in numerically solving six coupled vector equations obtained from Maxwell's equations in the time domain. The FDTD is a very powerful method and has been improved during the last decades to account for a great variety of problems in electrodynamics. However, it results heavily time-consuming, and requires large computer resources and even parallelization for very large simulation spaces [32].

In this paper, we present a very simple simulation method that allows studying the propagation of electromagnetic waves in a dielectric medium of arbitrary refraction index distribution. Due to its simplicity, the evolution of the propagating waves can be easily visualized on a conventional computer during runtime. One of the highlights of the proposed method is its versatility to obtain the optical response of an arbitrary dielectric photonic structure, which can be introduced within the simulation by means of a diagram or a photograph in a form of a digital image or bitmap. Then, the structure to be studied can be easily generated by means of any photo-editor software. In the case of natural photonic structures, an electron microscope image of the real specimen can be used.

In Sec. 2 we summarize the basic concepts of the simulation. Within the framework of the developed method, in Sections 3-6 we present a set of techniques which permit us to control and analyze the behavior of the waves within the simulation. We implemented a *direction filter* that permits decoupling waves travelling simultaneously in different directions, and also allows determining the field of energy flux in any type of wave (Sec.

3). In Sec. 4 we present an active system to cancel waves reflected at the edges of the simulation space, which allows simulating boundary conditions that represent an unbounded virtual space. This technique is independent of the wavelength and also works for any waveform, and then, it is capable of handling a multi-frequency excitation. Unlike other techniques to simulate perfectly absorbing boundary conditions, the proposed approach does not need to establish a finite thickness layer, and this constitutes one of its main advantages since it avoids wasting simulation space and time for that purpose. A multi-frequency excitation scheme based on a filter that allows decoupling of waves of several wavelengths travelling simultaneously is also shown in Sec. 5. Such a system increases the computing speed since it avoids making a sequential frequency sweep to obtain the spectral response of a given structure. Finally, in Sec. 6 we show how to obtain the far field (outside the simulation space) from the near field. As an example, in Sec. 7 we apply the simulation method, including the whole set of developed techniques, to obtain the optical response of the photonic structure present in the tissue of a microorganism. Concluding remarks are given in Section 8.

2. Description of the simulation

The simulation developed in this work is based on the method presented in [33] and reproduces the propagation of transverse mechanical waves. The correspondence between photonics and the behavior of mechanical waves have been already reported in the literature [34]. The physical model consists in a two-dimensional array of $p \times q$ particles of mass m contained in the $x - y$ plane. Each particle is joined to its four neighbors by means of elastic springs of elastic constant k and separated by a distance d. The movement of the particles is constrained to the z-axis, which is normal to the plane of the two-dimensional array, as shown in Fig. 1. The net force on each particle is null when it is located at $z = 0$. A wave (that will propagate along the $x - y$ plane) is generated by applying an external force along the z-axis to certain particles. The dynamic evolution of the system along time is obtained by means of an iterative algorithm based on an integration method of finite timesteps [33].

For large p and q, the array of particles can be considered as a continuous medium representing an elastic membrane subjected to a tension per unit length $T = F_e/l_T$, where F_e is the elastic force and l_T is the one-dimensional transversal section. The simulated membrane has a surface mass density

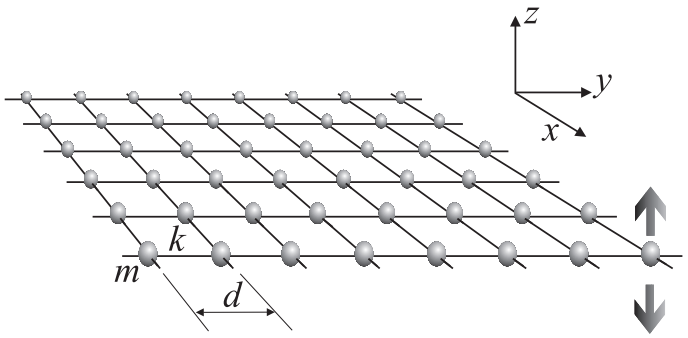


Figure 1: Particle array representing the physical model of the simulation.

$\mu = mN_m/s$, where m stands for the mass of the mesh element and N_m is the number of particles contained in a region of area s. For a medium with ground density mass μ_0, the speed of the waves is given by $v_0 = \sqrt{T/\mu_0}$. Therefore, in a region with a mass density $\mu > \mu_0$ the speed of the waves is $v < v_0$. Making an analogy with optics, regions with mass density μ_0 can be identified with vacuum, i.e., a medium of refraction index $n_0 = 1$, while a region with an arbitrary mass density μ corresponds to a medium with a real part of the refraction index $n = \sqrt{\mu/\mu_0}$. This approach permits to reproduce optical phenomena involving dielectric materials illuminated by transverse electric (TE) polarized light in two-dimensional configurations, and this has been verified for different systems and incidence configurations.

One of the remarkable features of this method is the possibility of defining the simulation domain by means of digital images or bitmaps. Each pixel in the image represents the position of the particle in the array. In this manner, a digital image of $p \times q$ pixels automatically defines the size of the simulation domain. An appropriate constant σ_p given in [nm/pixel] links the size of an object in the digital image, in pixels, with the actual physical size of the sample to be simulated, which is measured in nanometers.

Three bitmaps of equal size are defined within the simulation code to introduce different characteristics of the structure and the illumination conditions, which are denoted as M (mass density), D (damping) and E (excitation). The grey levels in the M bitmap represent the mass distribution within the array, which should be assigned using an adequate linear conversion function. Bitmap D encodes the damping constant of each point of the array, which allows introducing an attenuation constant in the medium, and bitmap E is introduced to specify the excitation, i.e., the particles on which

the external force is applied. Following the analogy with the propagation of electromagnetic waves in an optical medium, the M bitmap determines the refraction index distribution in space, bitmap D specifies the regions where there is absorption, and bitmap E specifies the location and shape of light sources. The grey level matrices M, D and E are related to the matrices M_{phys}, D_{phys} and E_{phys}, respectively, which contain the values of mass, damping and excitation measured in physical units, by:

$$M_{phys} = m_0 + M m_p, \tag{1}$$

$$D_{phys} = D \mu_p, \tag{2}$$

$$E_{phys} = r_p \, (E - 128), \tag{3}$$

where m_0 is the minimum mass value, which represents the refraction index of vacuum. The proportionality constant m_p in (1) has units of [kg/gl] and the constant μ_p has units of [N sec/(m * gl)]. Notice that [gl] is the grey level unit within a scale of 0-255 grey levels in which the digital images are represented. r_p in eq. (3) is a constant of units of [N/gl], which transforms the value of grey level provided by the bitmap E to a value of force. In eq. (3), a value $E = 128$ indicates that no force is applied on the particle. Then, values over 128 are interpreted as positive forces and grey levels values under 128 are interpreted as negative forces [33]. The harmonic excitation is introduced as

$$E_t = E_{phys} \sin{(\omega \, \tau_n \, n_c + \varphi)}, \tag{4}$$

where E_t is the applied external force, ω is the angular frequency of the excitation, φ is the initial phase and τ_n is a time adapting constant in units of [sec/cycle] that converts the integer number of iteration cycles n_c –which define the timestep–, into a physical time variable. The product $\tau_n \, n_c$ represents the discretized time variable, and the product $\omega_d = \omega \, \tau_n$ in eq. (4) can be regarded as a digitized angular frequency measured in [rad/cycle].

The Nyquist-Shannon sampling theorem [35] states that the frequency of the signal sampling must be at least twice the highest frequency component of the signal, in order to preserve the alternating nature of the external excitation after the sampling. In our case, the sinusoidal waveform of the externally applied force has a period 2π, and then it should be sampled as minimum at twice its frequency, that is, every π radians or less every iteration cycle. This implies that ω_d should be smaller than π rad/cycle. On the other

hand, the adapting constants τ_n and σ_p are related by

$$\tau_n = \frac{v_d}{v_{phys}} \sigma_p, \tag{5}$$

where v_d is the digitized speed of the waves (measured in [pixels/cycle]) and v_{phys} is the physical speed of the waves measured in [nm/sec]. In the case of optical waves in vacuum, $v_{phys} = v_0$ corresponds to $c = 2.99792 \times 10^{17}$ nm/sec. Therefore, the digitized angular frequency ω_d can be expressed as:

$$\omega_d = \omega \, \frac{v_d \, \sigma_p}{c}. \tag{6}$$

The above expression implies that once the optical frequency ω (or the optical wavelength λ) is fixed, the Nyquist-Shannon criterion requires

$$v_d \, \sigma_p < \frac{\pi c}{\omega}. \tag{7}$$

On the other hand, the Courant-Friedrichs-Lewy condition [36] imposes that v_{d0}, the digital counterpart of the maximum allowed speed v_0, must satisfy $v_{d0} \leq 1$ pixel/cycle. That is, the maximum allowed digitized wave speed that guarantees the stability of the simulation is one pixel per cycle of iteration. A speed beyond this value would cause the simulation to diverge. In other words, the dynamical information can be transferred to a maximum distance of one pixel, i.e., from one pixel to the next one, in each iteration cycle. This limit is not related to the computer processor speed or the physics of the modelled system. Instead, it ensures an internal logical consistency of the numerical method.

The proposed method allows studying the response of any two-dimensional distribution of refraction index in a very easy and practical manner. The refraction index distribution can be artificially generated using any available computational design tool for digital image edition, or it can be obtained from a digitized electron microscope image of a real physical structure. Recently, Kolle *et al.* implemented an interface for the MEEP package (an FDTD implementation) [37], which permits introducing the profile of the diffracting structure via binary images based on refraction index contrasts in SEM or TEM images [38].

Unlike other numerical methods in which the mathematical expression of the problem is known and the computer is used as a numerical integrator to obtain the solution, the idea behind the proposed simulation method is

the use of the computer as a generator of a virtual environment where the physical differential law is used to make the system evolve along the time, as it would evolve in the real physical world. The final solution is not predetermined by any mathematical expressions, but by the configuration and causality of the natural evolution of the introduced physical law. This way of thinking the problem has the advantage of naturally reproducing all the phenomena derived from the characteristics of the simulated medium and from the physical law involved. In this case, the simulated physical system is able to reproduce the whole family of linear wave phenomena, such as refraction, diffraction and interference, without having explicitly introduced any wave equation and/or boundary conditions [33].

3. Direction filter

As mentioned above, the proposed simulation has the advantage of genuinely reproducing the phenomena that would appear in a real physical system. However, at the same time, this advantage is the source of the main drawback of the method: its uncontrollability. For instance, spurious reflected waves will naturally appear at the edges of the simulation space. Incident and reflected waves will be superimposed, and this superposition makes it impossible to distinguish the amount of energy carried out by each one of the waves. The energy density then results from the interference of the incident and reflected waves. Besides, as it occurs in any experimental setup, within the simulation is not possible to determine the normal reflectance of a given sample under normally incident light, because the detector cannot be placed in the path of the incident light beam. And any artificial perturbation introduced in the movement of the particles within the mesh in order to decouple both waves, would affect the original (and actual) response of the system.

Fortunately, in contrast to what happens in the physical world, all the dynamical information of the system is known at every time in the simulation. This allows extracting this information in order to be processed in different ways. In the general case, multiple waves will be travelling simultaneously in different directions, producing a complex movement, and one would like to decouple these different components from the complex collective movement of the particles within the mesh. A method used to isolate a wave travelling in a given direction should be based on a natural way of processing the information in order to be able to work automatically for any wavelength,

amplitude, direction, waveform and, also, in the presence of an unknown number of other waves travelling in different directions.

At a first sight, this does not seem a trivial task and therefore the essential concept that represents a wave must be identified. A travelling wave of any wavelength, amplitude, direction or waveform has the following property: within a small region of space (small enough to be considered homogeneous), the waveform does not change in time, and only its phase changes at a known rate given by its phase velocity. In this context, we present a very simple and natural *direction filter* (*DF*) that allows extracting a wave travelling in a given direction and with a given sense. The filter is based on a wave subtraction technique and only uses as input parameter the speed of the wave to be filtered.

In order to present the direction filter in a clear way, in the following subsection we describe its formulation for one-dimensional problems and then, we present its extension to more dimensions.

3.1. Mathematical formulation of the DF *in 1D*

Suppose we have certain time-evolving function $A(x,t)$. Now, we propose the following operator:

$$\mathcal{F}^{(+)}[A(x,t)] = A(x,t+\Delta t) - A(x-v\Delta t,t), \tag{8}$$

where v is a constant representing a speed. If and only if $A(x,t)$ is a wave travelling at speed v towards the $+x$ direction, it must satisfy

$$A(x,t+\Delta t) = A(x-v\Delta t,t). \tag{9}$$

Substituting (9) in (8) we obtain

$$\mathcal{F}^{(+)}[A(x,t)] = A(x-v\Delta t,t) - A(x-v\Delta t,t) = 0 \quad \forall t. \tag{10}$$

$\mathcal{F}^{(+)}$ is called the *positive DF operator* acting on the wavefield $A(x,t)$ that cancels waves travelling towards the $+x$ direction. Correspondingly, $\mathcal{F}^{(-)} = A(x,t+\Delta t) - A(x+v\Delta t,t)$ is the *negative DF operator*, and it cancels waves travelling towards the $-x$ direction. In other words, the DF operator cancels a wave $A(x,t)$ travelling in a given direction by subtracting from it the same wave but evaluated in a previous instant and in a position displaced by an amount $\Delta x = v\Delta t$ from its present position. This is schematically shown in Fig. 2.

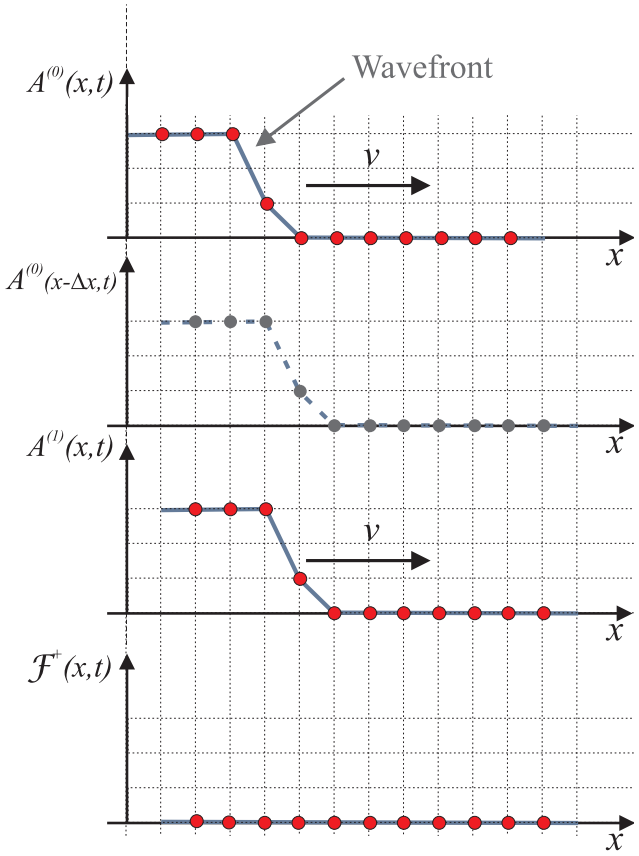


Figure 2: Geometric representation of the action performed by the *positive DF operator*.

Let us now evaluate the effect of the *positive DF operator* in a more general case (the analysis for the *negative DF operator* is completely analogous). Suppose that $A(x,t) = B^+(x,t) + B^-(x,t)$ is the superposition of two waves of arbitrary shapes travelling with speed v towards opposite directions $+x$ and $-x$, respectively. Taking into account that

$$A(x - v\Delta t, t) = B^+(x - v\Delta t, t) + B^-(x - v\Delta t, t) \tag{11}$$

and

$$A(x, t + \Delta t) = B^+(x, t + \Delta t) + B^-(x, t + \Delta t), \tag{12}$$

by applying $\mathcal{F}^{(+)}$ to this new function, we get:

$$\mathcal{F}^{(+)}[A(x,t)] = B^+(x,t+\Delta t)+B^-(x,t+\Delta t)-B^+(x-v\Delta t,t)-B^-(x-v\Delta t,t). \tag{13}$$

Since $B^+(x,t)$ and $B^-(x,t)$ are waves travelling towards the $+x$ and $-x$ directions, respectively, they satisfy

$$B^+(x, t + \Delta t) = B^+(x - v\Delta t, t) \tag{14}$$

and

$$B^-(x, t + \Delta t) = B^-(x + v\Delta t, t). \tag{15}$$

Therefore, the application of the *positive DF operator* results to be

$$\mathcal{F}^{(+)}[A(x,t)] = B^-(x + v\Delta t, t) - B^-(x - v\Delta t, t). \tag{16}$$

As expected, $B^+(x,t)$ is completely cancelled. By calling $x' = x + v\Delta t$, eq. (16) can be rewritten as

$$\mathcal{F}^{(+)}[A(x' - v\Delta t, t)] = B^-(x', t) - B^-(x', t - 2\Delta t), \tag{17}$$

which represents a wave travelling towards the $-x$ direction. By dividing both sides of eq. (17) by $2\Delta t$ and taking the limit $\Delta t \to 0$, eq. (17) can be expressed as:

$$\mathcal{F}^{(+)}[A(x,t)] \approx 2\Delta t \frac{\partial B^-(x + v\Delta t, t)}{\partial t}. \tag{18}$$

Expression (18) reveals the effect of the *DF operator* on a wave of general shape travelling in a non-filtered direction. For small Δt –compared with the time period of the higher harmonic component of $B^-(x,t)$–, the filtered wave is proportional to the time derivative of the original wave.

3.2. The Direction filter *in more dimensions*

In general electromagnetic scattering problems we have two- or three-dimensional wavefields, and then in this subsection we generalize the *DF* to more dimensions.

Consider a scalar wavefield $A_n(\mathbf{r},t)$ in a space of n dimensions. The general expression for the *DF operator* (8) in $\mathbb{R}^n$ is

$$\mathcal{F}_n^{(\mathbf{V},\delta)}[A_n(\mathbf{r},t)] = A_n(\mathbf{r},t+\Delta t) - A_n(\mathbf{r}-\mathbf{v}\delta,t), \tag{19}$$

This operator filters waves travelling with phase speed $|\mathbf{v}|$ in the direction of $\mathbf{v}$, with a characteristic time delay $\Delta t = \delta$. Note that bold letters represent vectors. To find out the effect produced by the *DF operator* on waves travelling in directions different from the filtering direction defined by $\mathbf{v}$, we consider a wavefield $A_2(\mathbf{r},t)$ in $\mathbb{R}^2$, in which case the *DF operator* (19) becomes

$$\mathcal{F}_2^{(\mathbf{V},\delta)}[A_2(\mathbf{r},t)] = A_2(\mathbf{r},t+\Delta t) - A_2(\mathbf{r}-\mathbf{v}\delta,t). \tag{20}$$

If the wavefield is a two-dimensional plane wave

$$A_2(\mathbf{r},t) = A\, e^{i\,\mathbf{k}_w(\mathbf{r}-\mathbf{v}_w\,t)}, \tag{21}$$

where $\mathbf{k}_w$ is the wave-vector, $\mathbf{v}_w = \omega/|\mathbf{k}_w|\,\mathbf{k}_w$ is the velocity of the wave and ω its angular frequency, substitution of (21) into (20) yields

$$|\mathcal{F}_2^{(\mathbf{V},\delta)}(\alpha)| = A\,|e^{-i\,\omega\,\delta} - e^{-i\,\omega\,\delta\,\cos(\alpha)}|, \tag{22}$$

where $|\mathcal{F}_2^{(\mathbf{V},\delta)}(\alpha)|$ is the complex amplitude of the filtered wave and α is the angle between the propagation direction ($\mathbf{k}_w$) and the filtering direction ($\mathbf{v}$) (see Fig. 3).

To quantify the performance of the DF, we define the relative attenuation μ_a of the wave as

$$\mu_a(\alpha) = 1 - |\mathcal{F}_2^{(\mathbf{V},\delta)}(\alpha)|/|\mathcal{F}_2^{(\mathbf{V},\delta)}|^{\max}, \tag{23}$$

where $|\mathcal{F}_2^{(\mathbf{V},\delta)}|^{\max}$ stands for the maximum value of $|\mathcal{F}_2^{(\mathbf{V},\delta)}(\alpha)|$ for $\alpha \in [0, 360^\circ]$.

Figure 4 shows the relative attenuation of a plane wave as a function of α. As expected, the maximum attenuation is obtained for $\alpha = 0$, that is, when the propagation direction of the plane wave coincides with the filtering direction. Conversely, the attenuation is minimum for the wave travelling in the opposite direction, that is, for $\alpha = 180^\circ$. In Fig. 5 we show the performance of the *DF* for a circular wavefront, which can be regarded as a superposition of plane waves propagating along all directions. The amplitude of the obtained filtered wave is shown in grey levels.

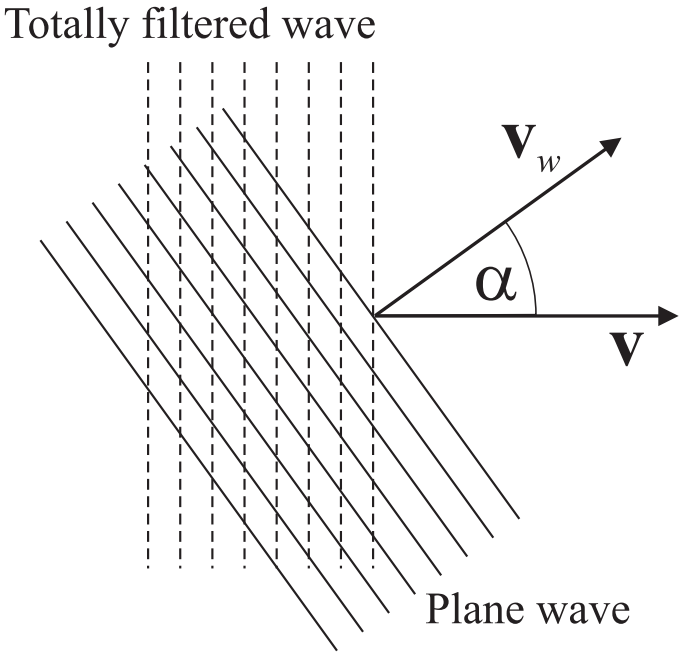


Figure 3: Angle α between the direction of propagation of the plane wave (along $\mathbf{v}_w$) and the filtering direction (along $\mathbf{v}$).

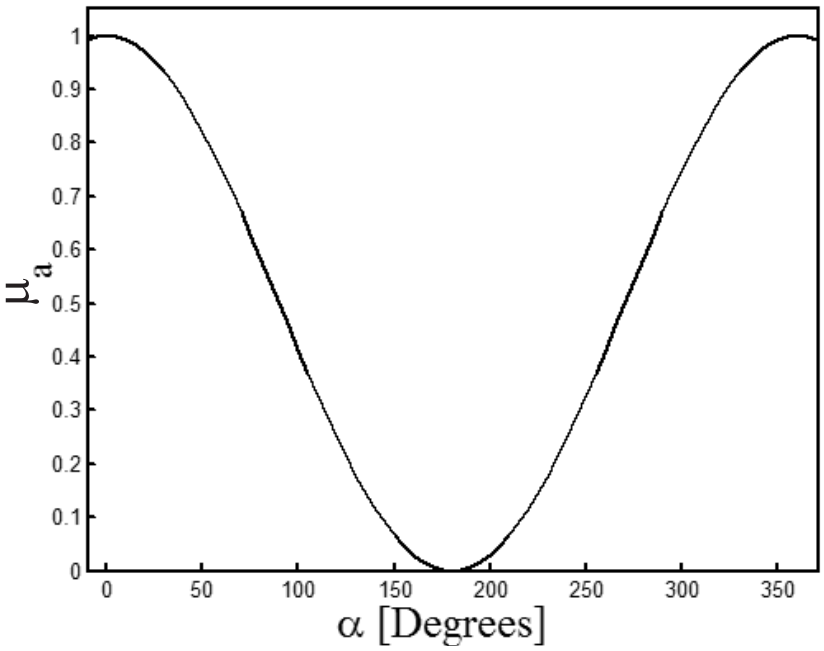


Figure 4: Attenuation of the plane wave as a function of the angle α between its direction of propagation and the filtering direction.

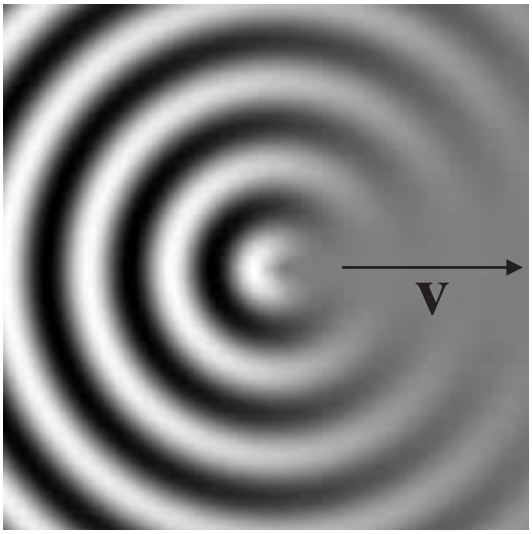


Figure 5: Angular effect of the *DF* on a circular wavefront.

3.3. Direction filter *implementation within the computer simulation*

As presented above, the *DF* is characterized by two parameters: $\mathbf{v}$, which determines the speed and direction of the wave to be filtered, and δ, the characteristic delay. As in any digital simulation, the space-time domain is discretized and then, this discretization imposes certain constrains on the *DF* parameters.

From eq. (20) it becomes evident that the filtering operation will be effective if the spatially displaced $A_2(\mathbf{r} - \mathbf{v}\delta, t)$ has exactly the same shape as $A_2(\mathbf{r}, t + \Delta t)$. Since in the discretized domain the minimum separation distance is 1 pixel, and the simulation allows a maximum digitized wave speed $v_{d0} \leq 1$ pixel/cycle (according to the Courant-Friedrichs-Lewy condition), the travelling wave advances a distance $d_0 = vt = v_{d0} \times \Delta n_c \leq 1$ pixel in one iteration cycle ($\Delta n_c = 1$), and therefore, $A_2(\mathbf{r}, t + \Delta t)$ will have the same shape as $A_2(\mathbf{r} - \mathbf{v}\delta, t)$ exactly after $1/v_{d0}$ iteration cycles, with $(1/v_{d0}) \in \mathbb{Z}$. During intermediate iteration steps, the wave will take interpolated values between $A_2(\mathbf{r} - \mathbf{v}\delta, t)$ and $A_2(\mathbf{r}, t + \Delta t)$ that will not exactly match the shape of neither of them.

According to this, the necessary requirement for a good performance of the *DF* within the simulation is that the speed of the waves must be set to $v_{d0} = 1$ pixel$/\Delta n_c$, with $\Delta n_c \in \mathbb{Z}$ being the integer number of iteration cycles in which the wave advances a distance of exactly 1 pixel. Therefore, the characteristic delay of the filter must be $\delta = \Delta n_c = 1$ pixel$/v_{d0}$ for a spatial shifting of $A_2(\mathbf{r} - \mathbf{v}\delta, t)$ equal to 1 pixel. In our simulations we usually set the second allowed digitized speed $v_{d0} = 0.5$ pixels/cycle, (i.e. $\Delta n_c = 2$). Therefore, in this case $\delta = 2$ cycles for a spatial shifting of 1 pixel in $A_2(\mathbf{r} - \mathbf{v}\delta, t)$. Although we could eventually use spatial shiftings larger than 1 pixel, larger shiftings lead to larger values of the characteristic delay δ, during which the shapes of $A_2(\mathbf{r} - \mathbf{v}\delta, t)$ and $A_2(\mathbf{r}, t + \Delta t)$ would be more affected by the numerical errors, thus decreasing the quality of the directional filtering.

It is worthwhile to mention that the above conditions are valid for the implementation of the *DF* in the orthogonal directions x and y, which coincide with the rows and columns of the discretized array of particles comprising the simulation medium, as shown in Fig. 1. In the present paper we use four *DF*s corresponding to the directions $+x$, $-x$, $+y$ and $-y$. From a practical programming point of view, the *DF* is applied to the waves evolving in the two-dimensional array defined by the simulation, called *main plane*. However, the resulting directionally filtered waves are stored in *secondary planes*.

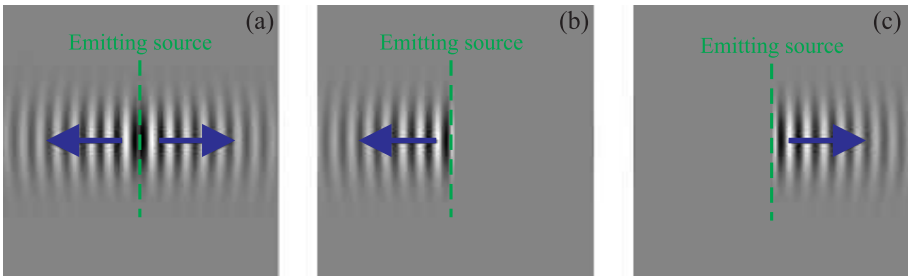


Figure 6: (a) Source emitting gaussian waves in directions $+x$ and $-x$. (b) *Secondary plane* of the *DF* that cancels waves travelling towards the $+x$ direction. (c) *Secondary plane* of the *direction filter* that cancels waves travelling towards the $-x$ direction. Blue arrows show the propagation direction of the wavefronts.

These *secondary planes* show time-evolving waves that are filtered images of the waves evolving in the *main plane*, and therefore, the *DF* does not affect the physics of the system. In this case, we have four secondary planes that store the filtered waves travelling in the $+x$, $-x$, $+y$ and $-y$ directions, respectively.

To illustrate the behavior of the *DF*, in Fig. 6(a) we show the *main plane* of the simulation of a linear source emitting gaussian waves in both directions $\pm x$. Figures 6(b) and 6(c) show the *secondary planes* that contain the wavefield of Fig. 6(a) after the application of the *DF* that cancels waves travelling towards the $+x$ and the $-x$ direction, respectively.

3.4. Determination of the energy flux vector field

One of the main applications of the *DF* presented in the previous subsections is the method for evaluating the energy flux of any simulated wavefield. This method makes use of the waves filtered in the orthogonal directions $\pm x$ and $\pm y$. Let us call I_{x+}, I_{x-}, I_{y+} and I_{y-} the intensity (calculated as the time integration of the square of the amplitude) of the waves travelling towards the $+x$, $-x$, $+y$ and $-y$ directions, respectively. Then, the quantities

$$\phi_x = I_{x+} - I_{x-} \tag{24}$$

and

$$\phi_y = I_{y+} - I_{y-} \tag{25}$$

are proportional to the energy flux along the x and y directions, respectively. Consequently, the vector field $\mathbf{F}$ defined as

$$\mathbf{F} = (\phi_x, \phi_y) \tag{26}$$

is proportional to the energy flux vector field.

According to (18), the filtered intensities are not equal to the intensity of the original wavefield, but proportional to its derivative. However, to determine the direction of the energy flux –and not its absolute value–, it is enough to compute the relative intensities between the filtered waves.

As an example, let us calculate ϕ_x for a wave $Z(\mathbf{r}, t)$ travelling along the $+y$ or the $-y$ direction. Since

$$\mathcal{F}_2^{(+x,\delta)}[Z(\mathbf{r}, t)] = \mathcal{F}_2^{(-x,\delta)}[Z(\mathbf{r}, t)], \tag{27}$$

i.e., the DFs for the $+x$ and $-x$ directions produce the same attenuation on waves that propagate along a direction orthogonal to their corresponding directions of filtering (see eq. (22)), according to (24) ϕ_x becomes

$$\phi_x = I_{x+} - I_{x-} = \int (\mathcal{F}_2^{(+x,\delta)})^2 dt - \int (\mathcal{F}_2^{(-x,\delta)})^2 dt = 0. \tag{28}$$

As expected, there is no energy flux along the x direction for the evaluated wave.

It should be mentioned that the DF developed here could also be applied to experimental data. For instance, the method of *Fourier transform profilometry* presented in [39] permits digitalizing the evolution of surface water waves along time. Therefore, the technique proposed in this paper also enables the calculation of the energy flux field for real systems.

4. Dynamic differential absorber

It is well known that any computer wave simulation can only reproduce the propagation of waves in a finite domain. Therefore, the waves arriving to the edges of the simulation domain will be naturally reflected back [33]. In order to simulate open boundaries, it is necessary to artificially cancel all the waves reflected at the edges of the simulation space. For this purpose, several methods have been proposed [33, 40, 41], each of them having its advantages and disadvantages. One possibility to avoid these reflections is to place a slab of an absorbing medium adjacent to the edges of the domain. In its basic implementation, this approach reduces the reflected waves, but it does not completely cancel them [33]. Besides, the absorbing region produces an unnecessary increment of the size of the simulation space and, consequently, the computation time also increases.

A highly improved version of the procedure described above is the so called *perfectly matched layer* (PML) method [30, 41]. This method is the most widely spread technique to cancel reflected waves, and it consists in introducing an absorbing anisotropic layer at the edges of the simulation space. Within this layer, the differential wave equation is modified by including a special transformation that produces a rapid attenuation of the wave as it propagates. Although this method results to be very efficient, it requires a layer of finite thickness to allow the decay of the waves. Besides, waves travelling parallel to the layer are not attenuated by the PML method, producing the accumulation of non-realistic energy in that region.

In this Section we present an alternative approach to simulate the open space by cancelling reflected waves at the edges of the simulation domain. The method, called *dynamic differential absorber* (DDA), is based on an intuitive concept, and its main advantage is that it does not require a layer of a given thickness to cancel the waves, i.e., it produces the absorption of the wave within a layer of infinitesimal thickness, and this saves computation space and time. On top of that, the method automatically cancels waves of any amplitude, shape or frequency with the same efficiency, and this constitutes a great advantage that enables the use of multi-frequency excitation, as shown in Section 5. As in the case of the *DF*, only the velocity of the incoming waves should be specified. It is important to mention that this method can be applied to waves of any nature, i.e., mechanical, electromagnetic, and potentially even to quantum waves governed by Schrodinger's equation.

In the following subsection we present the basic idea by means of the 1D formulation of the DDA, called here the *simple dynamic differential absorber* (SDDA). Then, we develop the *adaptive dynamic differential absorber* (ADDA), which is a generalization to two or more dimensions, and in which case the direction of the incoming waves must be taken into account.

4.1. Simple dynamic differential absorber (SDDA)

Consider a wave propagating along the x-axis towards the $+x$ direction, and let us examine the movement of this wave at two fixed points $x = x_a$ and $x = x_b$, as shown with the blue dots in Fig. 7. As the wave passes through, the amplitude A_b at x_b will take the value of A_a at x_a, but with a time delay given by $\Delta t = \Delta d/v_w$, where $\Delta d = x_b - x_a$ and v_w is the phase velocity of the wave. Within this context, the term "amplitude" refers to the magnitude of the wavefield at a given point.

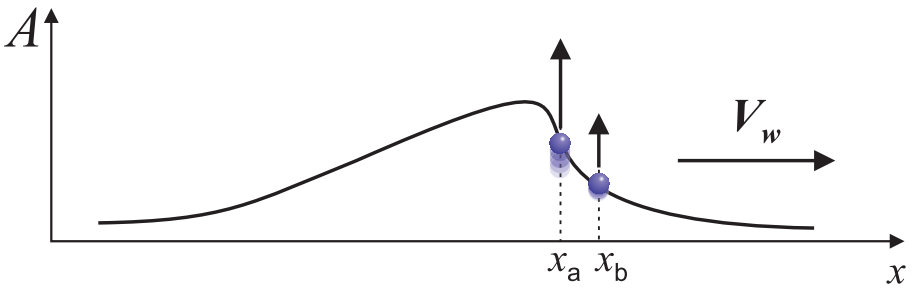


Figure 7: Amplitude of a propagating wave at two fixed points located in $x = x_a$ and $x = x_b$.

The key idea is the following: if we artificially control the amplitude A_b of the wave at x_b and make it move in such a way that A_b copies the amplitude A_a with the right time delay, the behavior of the propagating wave for $x < x_b$ will not be affected as it passes through. In fact, if x_b is a point located at the edge of the simulation domain, the incoming wave will not be affected at this point and it would continue propagating as if there were no boundary. Therefore, the SDDA consists in controlling the movement of a point located at x_b, called the *absorbing* point, according to the behavior of the incoming wave at x_a, called the *reading* point. Mathematically, we can exprees this procedure as

$$A_b^{(t_1)} = A_a^{(t_0)}, \tag{29}$$

where $A_b^{(t_1)}$ is the amplitude of the wave at x_b in a certain instant t_1, $A_a^{(t_0)}$ is the amplitude of the wave at x_a in a previous instant $t_0 = t_1 - \Delta t$, where $\Delta t = \delta_d \ \Delta d$. In this context, $\delta_d = 1/v_w$ is the *differential delay* which depends on the medium characteristics via the phase velocity of the waves within the propagating medium.

Although the above equations indicate that the *reading* point can be located arbitrarily close to the *absorbing* point, within the simulation method the discretized nature of the space-time domain must be taken into account, as already explained in subsection 3.3 for the *DF*. Since the minimum distance between the *reading* and the *absorbing* points is of one pixel, we also set the allowed digitized wave speed $v_{d0} = 0.5$ pixels/cycle (see subsection 3.3), and then $\delta_d = 1/v_{d0} = 2$ iteration cycles. If, for instance, a 1D simulation space is M pixels long, the rightmost pixel $m = M$ is forced to move as:

$$A_M^{(n_c)} = A_{M-1}^{(n_c-2)}, \tag{30}$$

where $A_{M-1}^{(n_c-2)}$ is the amplitude of the wave at the pixel $M-1$ stored two iteration cycles before the present cycle n_c. Similarly, the leftmost pixel $m'=1$ is forced to move as:

$$A_1^{(n_c)} = A_2^{(n_c-2)}, \tag{31}$$

where $A_2^{(n_c-2)}$ is the amplitude of the second pixel stored two iteration cycles before the present cycle n_c.

4.2. Adaptive dynamic differential absorber (ADDA)

If the simulation domain is two-dimensional, the SDDA presented in the previous subsection would only be effective for waves propagating normally to the edge of the simulation space (or whose wavefronts are parallel to the edges of the domain). In order to develop a direction-sensitive method that could properly absorb waves propagating with different directions, small corrections must be introduced into the *differential delay* used to cancel the incoming waves.

The effective wavelength λ_{eff} of the wave that arrives at the edge of the simulation space is given by

$$\lambda_{\text{eff}} = \lambda_w / \cos(\alpha), \tag{32}$$

where λ_w is the actual wavelength of the incoming wave and α is the angle between the direction of propagation and the normal to the edge of the simulation space. Then, the effective phase velocity v_{eff} –the phase velocity of the wave along the direction normal to the edge of the simulation space–, depends on the angle of incidence and is given by:

$$v_{\text{eff}} = \frac{\omega}{k_{\text{eff}}} = \lambda_{\text{eff}} f, \tag{33}$$

with $\omega = 2\pi f$, k_{eff} being the effective wavenumber and f the frequency of the wave. This is schematically shown in Fig. 8. Consequently, the *effective differential delay* δ_{eff} becomes

$$\delta_{\text{eff}} = \frac{1}{v_{\text{eff}}} = \frac{\cos(\alpha)}{v_w} = \delta_d \cos(\alpha), \tag{34}$$

which implies that δ_{eff} is always smaller than δ_d.

To determine δ_{eff}, the *reading* point must provide information not only about the time-varying amplitude of the wave to be cancelled, but also about

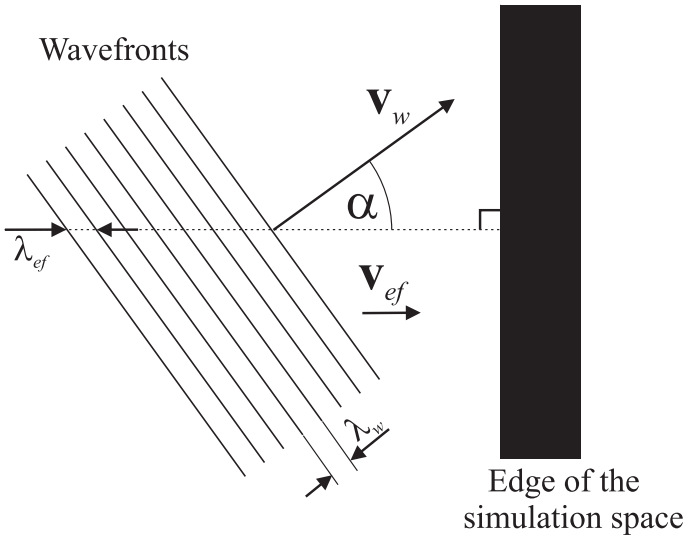


Figure 8: Effective wavelength λ_{eff} and effective phase velocity v_{eff} of an obliquely incident wave forming an angle α with the normal to the simulation space edge.

its direction of propagation, given by α. This angle can be obtained by evaluating the energy flux vector at the *reading* point, using the method described in subsection 3.4. For example, for the right hand-side edge of the simulation space, α is given by

$$\alpha = \arctan(\frac{\phi_y}{\phi_x}), \tag{35}$$

where ϕ_x and ϕ_y are the $x-$ and $y-$components of the energy flux, defined in eqs. (24) and (25). In practice, to clearly establish the direction of the incoming wave before it is affected by the edge of the simulation space, the information about the direction of the incoming waves is taken from points located between 2 and 4 pixels away from the edge of the simulation space, where the absorbing points are located. On the other hand, the discretized nature of the simulation must be taken into account. If the wave speed is set to $v_{d0} = 0.5$ pixels/cycle, δ_{eff} is a real number between 2 and 0 for α between 0 and 90°, respectively. Since the number of cycles δ_{eff} must be an integer, the resulting value Δt must be approximated to the closest integer value. This implies that the allowed discretized delays ($\delta_{\text{eff}} = 2$, 1 and 0) will only match the required delay for three angles of incidence, that in this case are $\alpha = 0°$, 60° and 90°. Therefore, in order to increase the number of allowed

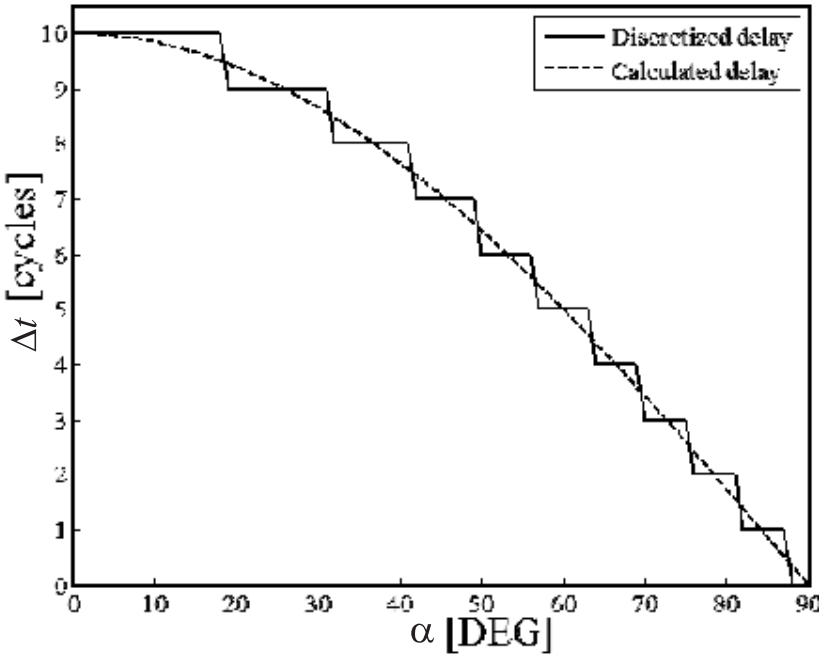


Figure 9: Delay vs. angle of incidence: discretized (solid line) and calculated (dashed line).

discretized delays, the wave speed can be decreased, and set, for instance, to $v_{d0} = 0.1$ pixels/cycle. In this case, δ_{eff} will be bounded between 10 and 0, for α between 0° and 90°, respectively. Then, the number of discretized delays is increased, and the error between the calculated and the allowed integer delays is minimized, as shown in Fig. 9. Increasing the number of discretized delays improves the effectiveness of the ADDA. Then, to increase the number of discrete delays we can either increase the distance between the *reading* and the *absorbing* point, or decrease the wave speed v_{d0}. Depending on the requirements of speed and usable space size of the simulation, the best choice should be made. Figure 10 shows the location of the *absorbing* points (in blue) and the *reading* points (in red) for a two-dimensional space. The distance Δd (magnified for clarity) between the *reading* and the *absorbing* points is also indicated.

Despite the difference between the calculated and the discrete values of δ_d introduced for certain incidence angles by the discretization process, it was verified that these errors do not significantly affect the performance of the

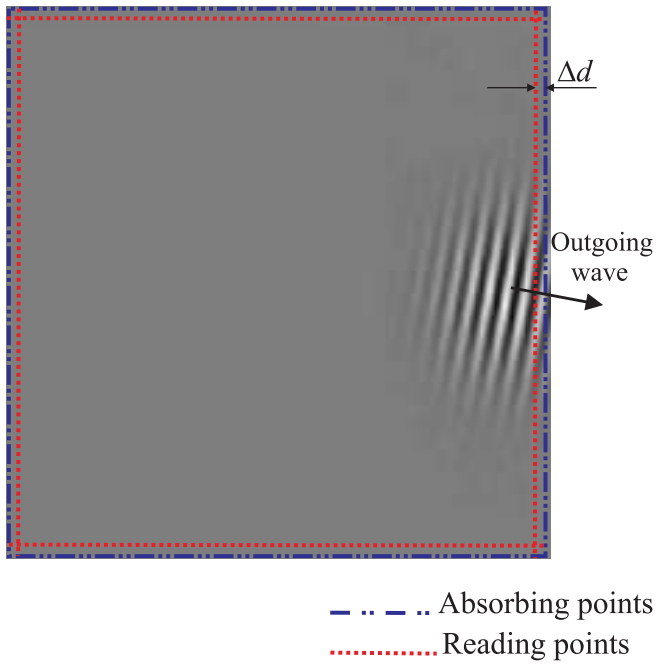


Figure 10: Location of the *absorbing* and the *reading* points for a 2D simulation space. The distance Δd is also indicated.

ADDA, even for $\delta_d = 2$ (second maximum digitized wave speed allowed) and $\Delta d = 1$ (maximum available space), as will be shown in the next subsection. Making an analogy with electronics, the proposed method behaves like an active device, which reads an input signal and reacts accordingly to return a post-processed output signal. In this sense, this method is different from most available absorbing methods, which behave like passive devices whose response does not take into account the input signal.

4.3. Validation

In order to evaluate the performance of the ADDA, the reflectance, defined as the ratio of the reflected to the incident intensity, was calculated for a gaussian beam incident on the edges of the simulation space with different angles.

In all cases, the distance between the *reading* and the *absorbing* points was set to $\Delta d = 1$ pixel. Figure 11 shows the reflectance as a function of the angle of incidence for $\delta_d = 2$ (blue line), $\delta_d = 4$ (green line) and $\delta_d = 8$ (red line).

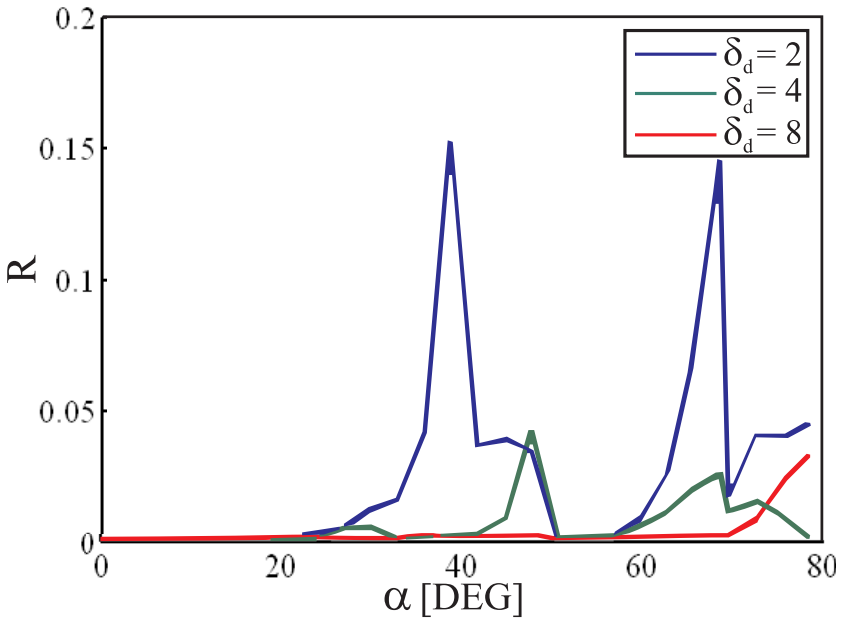


Figure 11: Numerical experiment with the ADDA: Reflectance vs. angle of incidence α for $\delta_d = 2$ (blue line), $\delta_d = 4$ (green line) and $\delta_d = 8$ (red line).

It can be observed that as δ_d is increased, the overall reflectance decreases, that is, a better performance of the absorber is obtained. For $\delta_d = 2$, there are peaks of relatively high reflectance for 39° and 69°. In the case of $\delta_d = 4$ the reflectance also shows peaks, but less intense than for $\delta_d = 2$. These peaks are located at the angles of incidence for which the difference between the calculated and the available integer delays is maximized. As the number of integer delays is increased (by increasing δ_d), a better matching between the calculated and the available integer delays is obtained (see Fig. 9), and the intensity of the reflectance peaks is gradually reduced, as observed for $\delta_d = 8$ in Fig. 11.

Figure 12 shows the attenuation produced by the ADDA expressed in decibels (dB), and calculated as $\chi = -10\ \log_{10}(R)$, where R is the reflectance. It can be noticed that for the angles for which the matching between the integer and the calculated delays is better, the attenuation values reach up to 44.2 dB for $\delta_d = 2$, 64.5 dB for $\delta_d = 4$ and 49.4 dB for $\delta_d = 8$. As a reference, the maximum attenuation values obtained with the PML applied within the FDTD method lie between 20 and 39 dB for small incidence angles, depending on the setting parameters of this method [41].

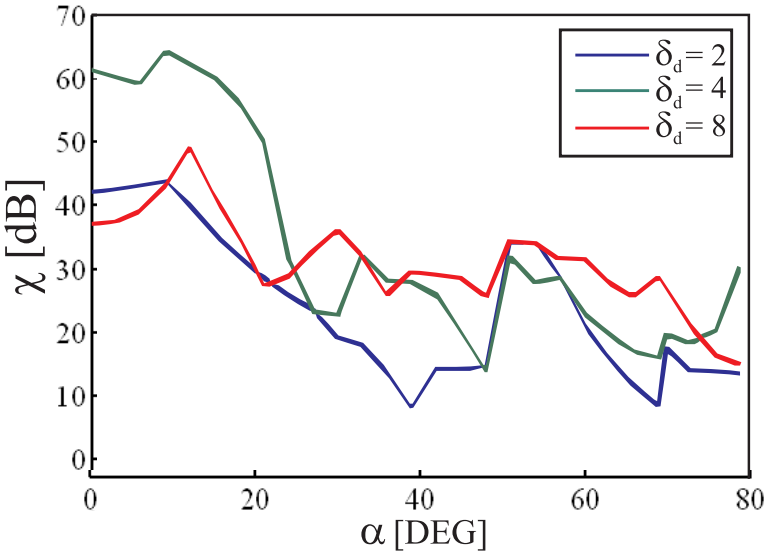


Figure 12: Attenuation vs. angle of incidence α for $\delta_d = 2$ (blue line), $\delta_d = 4$ (green line) and $\delta_d = 8$ (red line).

It can also be observed in Fig. 12 that for angles of incidence greater than approximately 25°, the best (larger) attenuation is obtained for $\delta_d = 8$, whereas for small angles of incidence the attenuation obtained for $\delta_d = 4$ is better. This result can be explained by taking into account that smaller angles of incidence require higher values of the effective differential delay δ_{eff}, as determined by (34). In this case, there are more iteration cycles between the *reading* and the *absorbing* instants for $\delta_d = 8$ than for $\delta_d = 4$. Then, if the sampling resolution of the shortest wavelength involved is low, a wave that propagates a fraction of pixel will be represented in the next timestep by a natural interpolation produced by the simulation. When the wave advances one pixel, the accumulated numerical errors produced by interpolation will be higher in the case of $\delta_d = 8$ than in the case of $\delta_d = 4$, producing a higher mismatch between the read waveform and the waveform that actually reaches the absorbing point. This produces a better performance for $\delta_d = 4$ for small angles of incidence. Therefore, in order to reduce the interpolation errors and improve the absorbing characteristics for small incidence angles, –i.e., for high differential delays δ_d,– the sampling resolution of the wavelengths comprising the wave to be cancelled must be increased, and this is done by decreasing the constant σ_p described in Section 2.

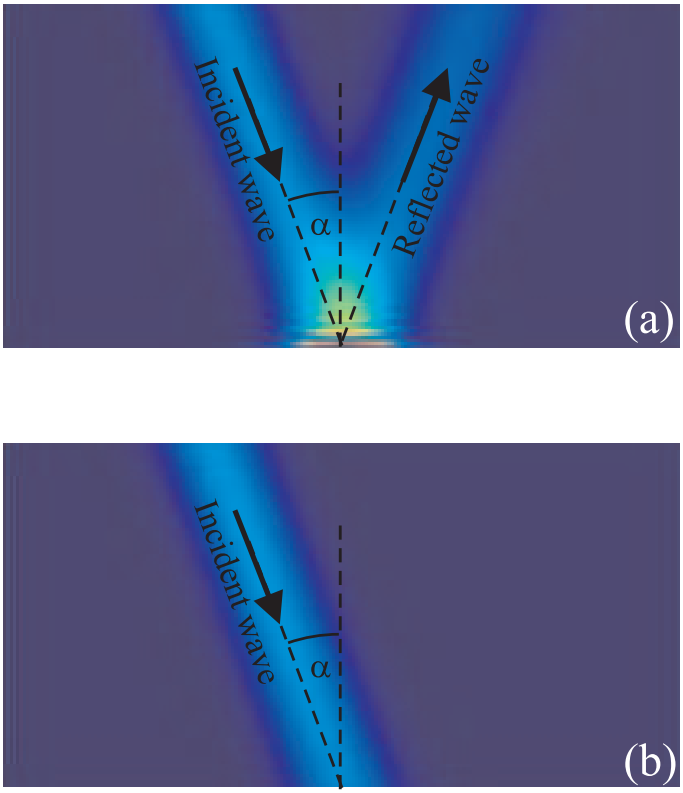


Figure 13: Intensity diagram of a gaussian beam forming an angle $\alpha = 20°$ with the normal to the lower horizontal edge of the simulation space for the case $\delta_d = 4$. (a) without ADDA; (b) with ADDA.

The effect of the ADDA is graphically shown in Fig. 13 for an incident gaussian beam forming an angle of 20° with the normal to the edge of the simulation space. Figure 13(a) shows the intensity diagram without the ADDA, where the reflected wave can be observed. On the other hand, Fig. 13(b) shows that the reflected beam is almost completely cancelled when the absorber is activated.

5. Tuning filter

The optical response of a structure is usually described by its reflectance and transmittance as a function of the wavelength. Therefore, in order to obtain its optical response using a simulation, the program should be executed for many frequency values and this could take considerable computing time,

especially if the desired spectral resolution is high. To avoid this problem, in this Section we show that a *multi-frequency excitation* (MFE) scheme can be implemented within the simulation in a quite straightforward manner.

Within this framework, the single frequency excitation (SFE) described in (4) is replaced by

$$E_t = \sum_{i=1}^{f_{\rm tot}} E_i \sin(\omega_i \, \tau_n \, n_c + \varphi_i), \tag{36}$$

where $f_{\rm tot}$ is the total number of frequencies, E_i is the excitation bitmap for the i-th frequency ω_i and φ_i is the i-th initial phase. In what follows we set $E_i = E$, meaning a uniform frequency spectrum.

Each point in the simulation space has a complex oscillating movement resulting from a mixture of the whole set of waves of different frequencies having unknown amplitudes, and we are interested in extracting each frequency component from the multi-frequency wavefield. One possible way to do this is to store the time evolution of the whole set of pixels in the simulation space in order to perform the Fourier transform for each pixel. Then, the spectral amplitude for each pixel can be obtained from the Fourier spectrum evaluated at any single frequency. The maximum number of iteration cycles used in each particular case depends on the size of the bitmap that defines the simulation space and on the setting of the digitized speed of the wave v_{d0}. In order to guarantee that the waves could reach every point within the simulation space, we established the following criterion: the total number of iteration cycles $n_c^{\rm tot}$ should be such that it ensures that a wave can travel twice the longest straight distance within the simulation space. For a bitmap of $p \times q$ pixels and a wave speed v_{d0}, the minimum number of cycles is:

$$n_c^{\rm tot} = 2 \, \frac{\sqrt{p^2 + q^2}}{v_{d0}}. \tag{37}$$

Therefore, to evaluate the Fast Fourier Transform (FFT) for each pixel, it would be necessary to store the complete evolution of the waves in a 3D matrix of size $(p, q, n_c^{\rm tot})$. Hence, for a 3D simulation space, a 4D matrix should be stored. For example, a 2D simulation space of 1 Mpixel would require to store a 21 GBytes matrix (with double precision), which exceeds the RAM memory of today conventional computers. On the other hand, in the FFT algorithm the frequency domain size equals the digitized time

domain size. Then, for a typical resolution of 10 nm in the wavelength, the set of points corresponding to the whole set of frequencies results to be very localized in the Fourier space, as shown in Fig. 14. Under these conditions, and due to the digitized nature of the Fourier space, the estimation of each spectral amplitude is highly inaccurate. In order to reduce the error, the size of the frequency domain should be enlarged by increasing even more the size of the digitized time domain n_c^{tot} given by eq. (37). Figure 14(a) shows the amplitude (in arbitrary units) of the time evolution of a pixel under multi-frequency excitation for 41 simultaneous waves of optical frequencies contained within the range 380 - 780 nm and using $n_c^{\text{tot}} = 10000$ cycles, $\tau_n = 3.335 * 10^{-17}$ sec/cycle and the same excitation amplitudes for all the frequencies. The amplitudes of the detected frequencies are very irregular, showing that the FFT is not useful to adequately isolate the amplitude of each frequency under these excitation conditions and digital resolution, as shown in the example of Fig. 14(b).

To solve this problem, we introduce the *tuning filter* (*TF*), that allows extracting a single-frequency time-varying wave from the multi-frequency wavefield. This filter acts as a temporal mask which is applied on the simulation space. After the application of the *TF* to the time-varying multi-frequency wavefield, a dynamic single-frequency wave can be visualized, allowing its processing to determine physical magnitudes such as reflectance or transmittance for a given frequency.

5.1. Implementation

The *TF* is based on the tuning properties of the forced damped oscillator, governed by the well known inhomogeneous differential equation

$$\frac{F_{\text{ext}}}{m} = \frac{d^2 z}{dt^2} + \gamma \, \frac{dz}{dt} + \omega_{do}^2 \, z, \tag{38}$$

where F_{ext} is the applied external force, z and t are the position and time variables, respectively, γ is the damping constant, and $\omega_{do} = \sqrt{k_{do}/m_{do}}$ is the natural frequency of the damped oscillator (k_{do} is the spring elastic constant and m_{do} is its mass). The *TF* uses the characteristic frequency response of the forced damped oscillator, which acts as a narrow band filter and maximizes the signal at resonance, i.e., when the frequency of F_{ext} equals the natural frequency ω_{do} of the oscillator. Under the condition $\gamma \ll \omega_{do}$, the width of the resonance peak is given by

$$\Delta\omega \approx \gamma, \tag{39}$$

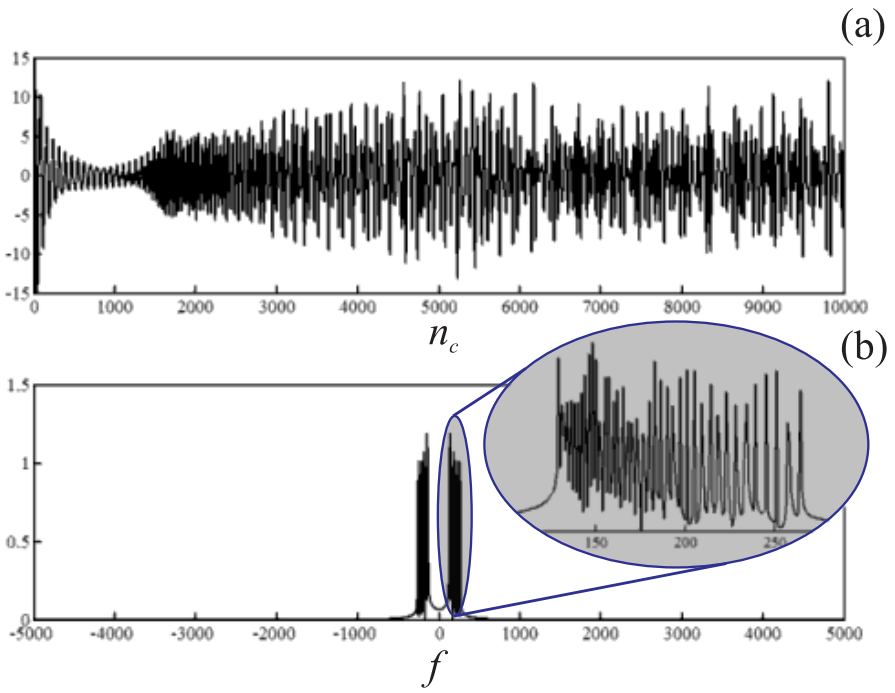


Figure 14: Multi-frequency excitation corresponding to 41 optical wavelengths contained within the range 380 - 780 nm, for $n_c^{\text{tot}} = 10000$ cycles, $\tau_n = 3.335 * 10^{-17}$ sec/cycle and equal magnitude of the external force applied to all the waves of different frequencies: (a) time evolution of a single pixel; (b) the absolute value of its FFT.

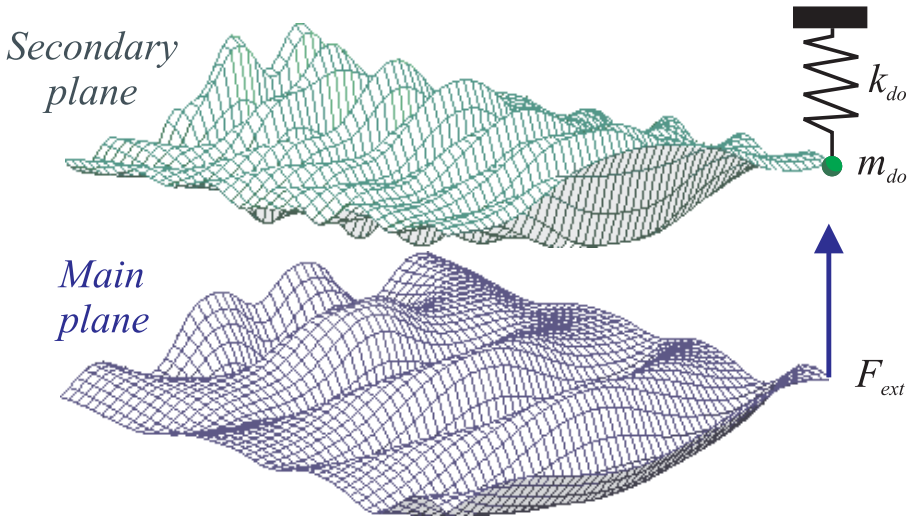


Figure 15: Schematic diagram of the tuning filter implementation.

the resonant frequency is given by

$$\omega_{\mathrm{r}} = \sqrt{\omega_{do}^2 - \frac{\gamma^2}{2}} \approx \omega_{do}, \tag{40}$$

and the sharpness of the resonance peak is determined by the quality factor Q, defined as

$$Q = \frac{\omega_{do}}{\gamma}. \tag{41}$$

Larger Q values correspond to sharper resonance peaks.

The implementation of the *TF* is similar to that of the *DF*. The simulation space where the multi-frequency wavefield is evolving is considered as the main plane. Then, a damped oscillator is associated to each point of the main plane, forming a two-dimensional array of oscillators, called the secondary plane. As schematized in Fig. 15, the wavefield amplitude at each point in the main plane is used to generate a proportional force that is applied to the particle of mass m_{do} in the corresponding oscillator. The displacement of each particle in the secondary plane is associated to the amplitude of the filtered wavefield. The oscillators are tuned at the frequency to be isolated, and then, the value of ω_{do} is selected accordingly. Therefore, as many secondary planes as frequencies to be extracted will be needed.

The main advantage of the MFE is that the computing time is significantly reduced compared with the SFE. In principle, the MFE employs the

same time to complete the simulation of the wavefield as that used by the SFE for just a single frequency. For a spectrum containing f_{tot} discrete frequencies, the total number of iteration cycles is reduced f_{tot} times with respect to the number of iteration cycles required to process the same signal when a sequential swept of f_{tot} single frequencies is carried out. However, the advantage in speed is compensated by a requirement of more memory to store the whole set of secondary planes and their respective auxiliary variables, which also introduces a slight delay in the computing time of each iteration cycle of the MFE compared with that of the SFE. This delay increases with the number of simultaneous frequencies explored in the MFE. More precisely, the computing times for a single iteration cycle within each excitation scheme are related by:

$$t_{\text{MFE}} = t_{\text{SFE}} \, (1 + \delta_{\text{MFE}} \, f_{\text{tot}}), \tag{42}$$

where δ_{MFE} is the additional fraction of t_{SFE} required by each frequency. In the case of the algorithm implemented in this work, $\delta_{\text{MFE}} \approx 0.03879$. In general, δ_{MFE} could vary according to the dynamic memory allocation efficiency of the implemented algorithm.

Taking into account (42), to run a whole set of frequencies the MFE requires less computing time than the SFE if

$$n_{cS}^{\text{tot}} > (1 + \delta_{\text{MFE}} \, f_{\text{tot}}) \, n_{cM}^{\text{tot}}, \tag{43}$$

where n_{cM}^{tot} is the total number of iteration cycles for the MFE and $n_{cS}^{\text{tot}} = f_{\text{tot}} \cdot n_c^{\text{tot}}$ is the total number of iteration cycles for the SFE.

While n_{cS}^{tot} is only determined by the size of the simulation space and by f_{tot}, in the case of the MFE n_{cM}^{tot} is also conditioned by the required selectivity of the *TF*, which depends on $\Delta\omega$ and on f_{tot}. According to (39), the separation between adjacent discrete frequencies should be $\Delta\omega \geq \gamma$ to perform an adequate isolation of frequencies. Besides, the *TF* should work under the stationary regime, i.e., when the non-tuned frequency oscillations have vanished. Since the time employed by the oscillator to reach the stationary regime is inversely proportional to γ, the time required by the *TF* to isolate the selected frequency basically depends on the desired resolution $\Delta\omega$. Consequently, the value of γ should be adjusted according to the speed and precision requirements of the simulation in each particular case, and this determines the value of n_{cM}^{tot}. According to the above considerations, one could decide which scheme is more appropriate.

5.2. Discretization requirements and validation

In the case of the optical spectrum ($\lambda \in [380\text{ nm}, 780\text{ nm}]$) discretized in steps of 10 nm (41 frequency values), the value of n_{cM}^{tot} required for an appropriate separation of frequencies results to be large since, in this case, $\Delta\omega = \gamma$ is small and then the required quality factor is very high (see eq. (41)). Moreover, to minimize the noise produced by the non-tuned components in the tuned frequency wave, it is even convenient to choose $\gamma \ll \Delta\omega$, and this implies a high value of n_{cM}^{tot}.

The total number of cycles n_{cM}^{tot} required by the *TF* to extract a frequency could, in principle, be reduced by increasing the time adapting constant τ_n (see eq. (4)), i.e., by increasing ω_d. As mentioned in Section 2, the Nyquist-Shannon criterion imposes $\omega_d < \pi$. However, it was found that for high values of ω_d the *TF* resonates at a frequency higher than the tuned frequency. Then, to ensure that the *TF* selects the desired frequency, ω_d must satisfy $\omega_d \ll \pi$, and therefore:

$$v_d\ \sigma_p = \frac{\omega_d\ c}{\omega} \ll \frac{\pi\ c}{\omega}, \tag{44}$$

for ω_d and ω being the maximum digitized and physical frequency contained in the analyzed spectrum, respectively.

In order to quantify the performance of the *TF* independently from other characteristics of the simulation, we define the relative error (in percentage) of the obtained intensity as a function of the explored wavelength as:

$$\varepsilon_r(\lambda_e) = 100\,\frac{|I_{\text{MFE}}(\lambda_e) - I_{\text{SFE}}(\lambda_e)|}{I_s(\lambda_e)|}, \tag{45}$$

where $I_{\text{MFE}} = (A_{\text{M}}^{\max})^2$ and $I_{\text{SFE}} = (A_{\text{S}}^{\max})^2$ are the intensities obtained with the MFE for the wavelength λ_e and the SFE, respectively, and $A_{\text{M}}^{\max}$ and $A_{\text{S}}^{\max}$ are the maximum amplitudes detected at the final stage of the time evaluation (in which the *TF* is in the stationary regime) for the MFE and the SFE cases, respectively.

The exploration of the optical spectrum with a resolution of 10 nm is an extreme situation for the MFE scheme because, as mentioned above, for 41 simultaneous frequencies a very high quality factor is needed, which leads to a very large number of iteration cycles n_{cM}^{tot}. This limitation can be overcame by exploring the same amount of frequencies in several MFE stages having a larger separation between frequencies, in such a way that different frequencies are covered in each stage. In this manner, the required quality factor of the *TF* is greatly decreased and therefore, n_{cM}^{tot} is also considerably reduced. For

example, the optical spectrum can be explored in five MPE stages with a resolution of 50 nm ($f_{\text{tot}} = 9$). In this case, an error of $\varepsilon_r = 5.25\%$ can be achieved with $n_{cM}^{\text{tot}} = 50000$ cycles per stage, $\gamma = 10^{-4}$ rad/cycle, $\sigma_p = 19$ nm/pixel and $v_{d0} = 0.5$ pixels/cycle. Therefore, the total number of cycles required to explore the 41 frequencies will be $5\, n_{cM}^{\text{tot}} = 250000$. For $\delta_{\text{MFE}} \approx 0.03879$, the MFE scheme becomes more suitable than the SFE in terms of computing time to explore the 41 optical frequencies, if the simulation space becomes larger than 1454×1454 pixels. This example shows that for large simulation spaces, the MFE (and the use of the *TF*) represents an advantage over the SFE, that can be implemented in any conventional computer. The decision on which scheme (MFE or SFE) is more suitable will in general depend on the maximum allowed error in each particular case.

If we are just interested in the visualization of the field associated to each frequency, less precision is required. In this case, the whole set of frequencies can be analyzed in a single stage, with a higher value of γ, which considerably reduces the required number of iteration cycles.

As an example, the field scattered by an opaque cylinder of diameter 620 nm was simulated for an incident optical multi-frequency plane wave ($\lambda \in$ [380 nm,780 nm], $\Delta\lambda = 10$ nm) with $\gamma = 10^{-4}$ rad/cycle, $\sigma_p = 20$ nm/pixel, $v_{d0} = 0.5$ pixels/cycle, and a simulation space of 150×150 pixels. Figure 16(a) shows the resulting multi-frequency intensity diagram for the scattered wavefield and Figs. 16(b)-(d), are the intensity diagrams for several extracted components of wavelengths 780 nm, 570 nm and 380 nm, respectively, for $n_{cM}^{\text{tot}} = 600$. The white dashed line denotes the cylinder position. As can be observed, even for a very low number of iteration cycles the *TF* allows a clear visualization of the wavefield of each frequency. This result can be explained by taking into account that if γ is relatively high, the non-tuned frequency components are rapidly damped and the filter would immediately be oscillating at its tuning frequency, although the stationary regime has not been strictly reached.

The possibility of getting a clear and rapid visualization of the selected frequency components by means of the *TF* could also be useful to decouple the different frequencies that coexist in a multi-frequency field of mechanical waves obtained experimentally. A few thousands of frames of an experimental evolving multi-frequency wavefield could be enough to decouple and visualize the evolution of a single frequency component. This feature also makes the *TF* a valuable tool for visualization and signal processing of experimental data.

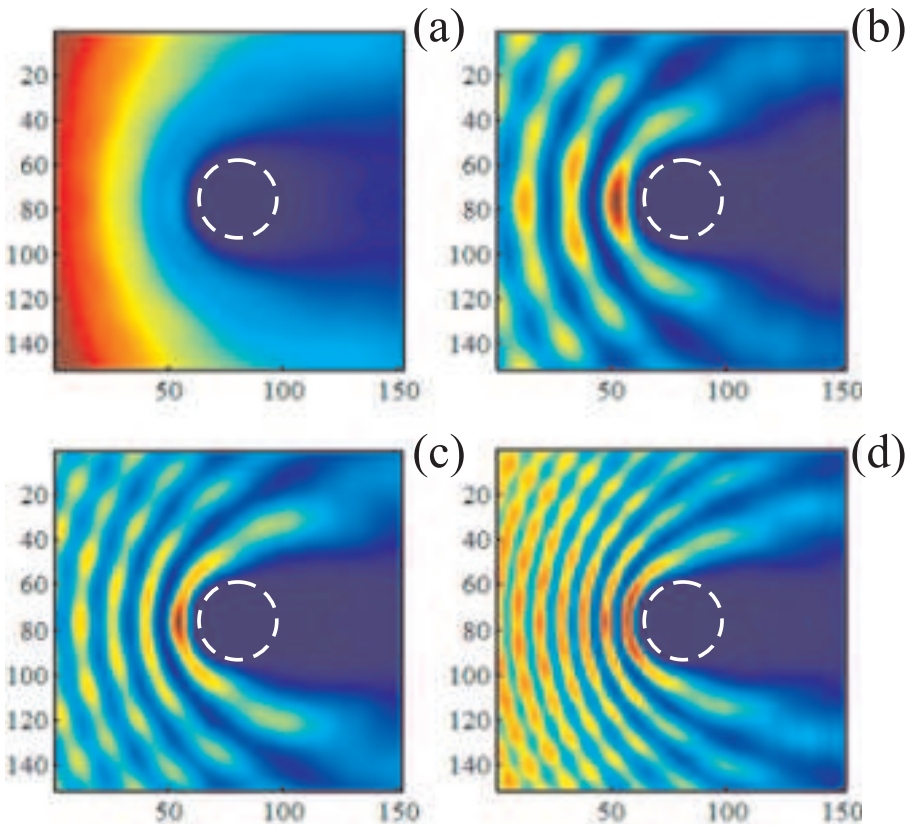


Figure 16: Simulated intensity diagram of a multi-frquency plane wave scattered by an opaque cylinder of a diameter of 620 nm. (a) The multi-frequency wavefield; (b) λ= 780 nm component; (c) λ= 570 nm component; (d) λ= 380 nm component.

6. Near-to-far-field transformation method

The method proposed in this work provides the near field distribution of a wave interacting with a given object. However, in many practical cases one is interested in the far-field response of an illuminated structure. On the other hand, there are many analytical methods that only provide the far field response of canonical problems, that could serve for validation and for appropriately setting the parameters of our simulation method. Therefore, in this Section we explain how the far field is obtained from the near field.

The transformation method used to obtain the far field from the near field is based on Green's Theorem [30, 42]. The remarkable advantage of this method is that it avoids the enlargement of the simulation domain to obtain the far-field information.

If the wavefield is represented by a complex phasor $Z(\mathbf{r},t) = Z_R(\mathbf{r},t) + i\, Z_I(\mathbf{r},t)$, according to Green's theorem [30] for a fixed time we have:

$$Z_t(\mathbf{r}) = \oint_{C_a} [G(\mathbf{r}|\mathbf{r}')\, \widehat{n}'_a \cdot \nabla' Z_t(\mathbf{r}') - Z_t(\mathbf{r}')\, \widehat{n}'_a \cdot \nabla' G(\mathbf{r}|\mathbf{r}')]\, dC', \tag{46}$$

where $Z_t(\mathbf{r})$ is $Z(\mathbf{r},t)$ evaluated at a fixed t, $\mathbf{r}'$ is the position of a source point over an arbitrary contour C_a enclosing the scatterer, $\widehat{n}_a$ is the outward unit normal to the contour C_a, $\mathbf{r}$ is an observation point outside C_a, and $G(\mathbf{r}|\mathbf{r}')$ is the Green's function, which in two dimensions is given by the Hankel function

$$G(\mathbf{r}|\mathbf{r}') = \frac{i}{4} H_0^{(2)}(k|\mathbf{r}-\mathbf{r}'|), \tag{47}$$

with i being the imaginary unit and $k = 2\pi/\lambda$ the wavenumber.

To apply eq. (46) and calculate the far field, we need to have the complex near field $Z_t(\mathbf{r})$ for each pixel. However, the present simulation method provides a real scalar wavefield, and then, its imaginary part should be found. Taking into account that

$$Z_{\mathbf{r}}(t) = A_{\mathbf{r}}(t) e^{-i\omega t} = A_{\mathbf{r}}(t)\cos(\omega t) - i\, A_{\mathbf{r}}(t)\sin(\omega t), \tag{48}$$

where $A_{\mathbf{r}}(t)$ is the amplitude of the phasor at a fixed position $\mathbf{r}$ and ω is the angular frequency in a steady state (when $A_{\mathbf{r}}(t)$ is constant), it is easily verified that

$$Z_I(\mathbf{r},t) = \frac{d}{dt}\{Z_R(\mathbf{r},t)\}\ . \tag{49}$$

Since the simulation provides $Z_R(\mathbf{r},t)$, we use (49) to calculate $Z_I(\mathbf{r},t)$ and therefore, to build the phasor for each pixel that is introduced into eq. (46) to calculate the far field.

7. Application example

In this Section we show an application of the proposed simulation and of the whole set of techniques developed in this work to obtain the optical response of a highly complex structure of biological origin. In particular, we evaluate the optical response of the peridium –a transparent protective layer that encloses the mass of spores– of the *Diachea leucopoda* (Physarales order, *Myxomycetes* class), which is a microorganism that has a characteristic pointillistic iridescent appearance (see Fig. 17(a)). It has been recently demonstrated that this appearance is of structural origin [18, 43]. We use a transmission electron microscope (TEM) image of the peridium cross section of the *Diachea leucopoda*, shown in Fig. 17(b), to set the M bitmap, which defines de refraction index distribution by means of a linear conversion of the grey levels of the negative image of Fig. 17(b). The grey level 0 (black) is associated to the lowest value of the refraction index (equal to unity). The average refraction index of the peridium was set to 1.78, which corresponds to a common value found in biological tissues. The optical source is a gaussian beam of width 2 μm. 41 optical frequencies were explored in the range 380-780 nm with a spacing of 10 nm. The simulation space was set to be of 280 $\times$ 230 pixels and $\sigma_p = 15$ pixel/nm. The width of the sample obtained from the TEM image is 1.68 μm and its mean thickness is 550 nm. In order to avoid errors produced by the finite size of the peridium image, we extended the biological slab at both sides by planar homogeneous slabs whose thickness is the average thickness of the actual image and whose refraction index is its average refraction index.

Figure 18 shows the resulting near field distribution of reflected intensity produced by the peridium cross section for a wavelength of 380 nm, and Fig. 19 shows the total far field reflectance as a function of the observation angle α and of the wavelength λ (the color scale bar is the same for Figs. 18 and 19).

8. Conclusion

In this paper we presented an electromagnetic wave simulation method to obtain the time-varying fields for multi-frequency excitation and arbitrary shapes and refraction index distribution of dielectric objects. This method results particularly suitable for investigating the electromagnetic response of photonic structures of biological origin, that usually present a high degree

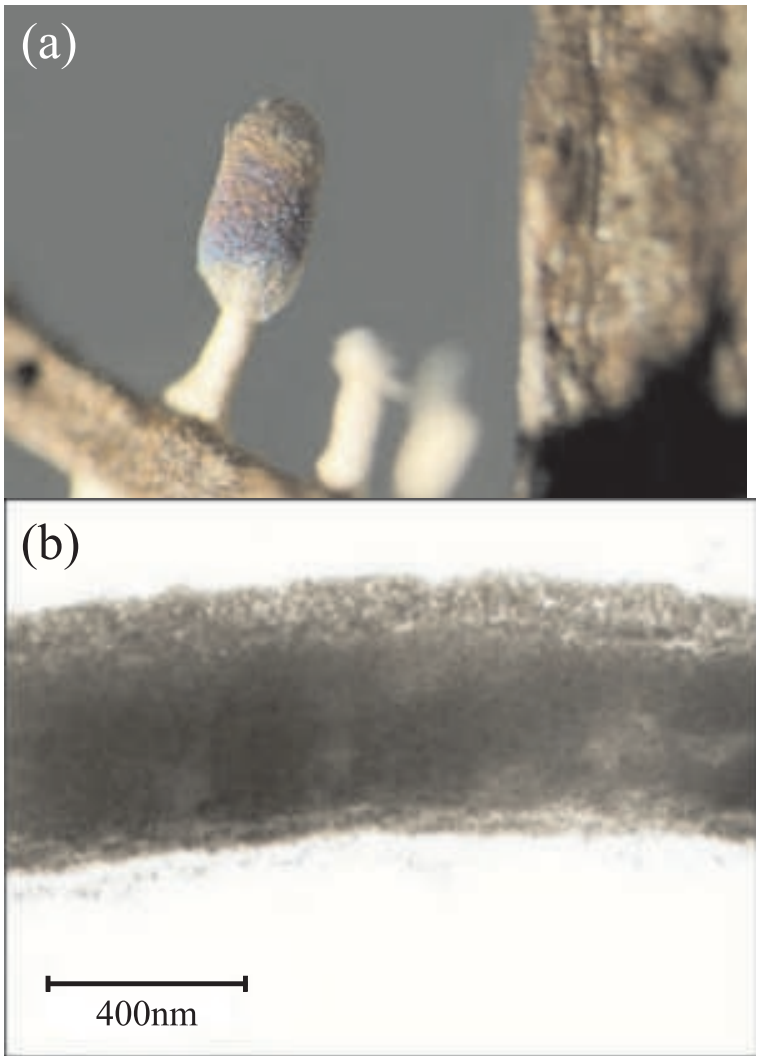


Figure 17: (a) *Diachea leucopoda* observed under the optical microscope and (b) transmission electron microscope image of the peridium cross section.

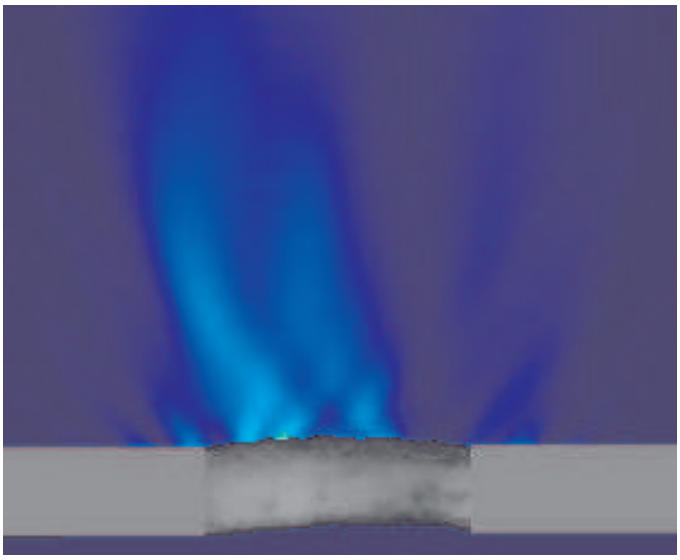


Figure 18: Reflected near-field intensity diagram produced by the peridium of the *Diachea leucopoda* obtained with the simulation method, for a wavelength of 380 nm.

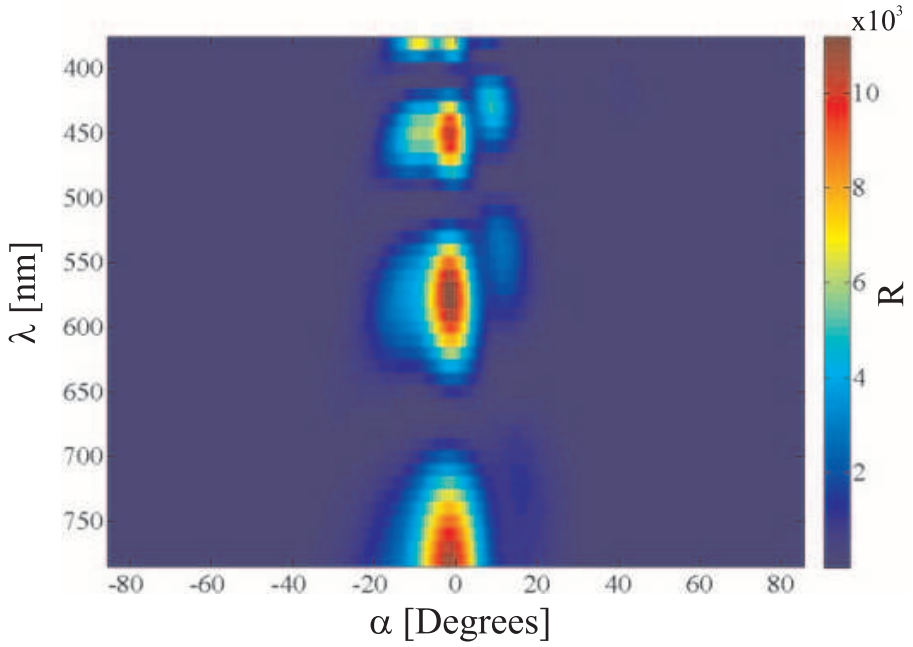


Figure 19: Far-field reflectance (R) as a function of the observation angle α and of the wavelength λ for the peridium of the *Diachea leucopoda*.

of complexity in their geometry as well as in the materials involved. To improve the performance of the method from the point of view of computing time optimization and space saving, we implemented a set of techniques that permit us controlling and analyzing the propagating waves within the simulation. These methods include a direction filter, that permits decoupling waves travelling in different directions, a dynamic absorber, that prevents the reflection of waves at the edges of the simulation space in order to reproduce unbounded spaces, and a tuning filter that allows multi-frequency excitation. We also adapted a near-to-far field method to calculate the far field with a minimum use of computation time and allocation space. Also, possible applications of these techniques have been suggested to analyze time-varying experimental wavefields. As an application example, we calculated the reflectance of the transparent cover layer of a microorganism that exhibits iridescence, for multiple wavelengths and observation angles.

In its present form, the proposed simulation method computes the electromagnetic response in the case of transverse electric (TE, electric field perpendicular to the plane of incidence) polarized incident light. In order to fully simulate the electromagnetic response of complex structures with traslational invariance, also the transverse magnetic polarization mode (TM, magnetic field perpendicular to the plane of incidence) should be included. This would require an extension of the method to a fully vectorial formulation, that is already under development. Another aspect in which we are planning to work in the near future is the extension of the simulation to deal with three-dimensional objects. As stated above, most biological structures are highly complex and require a 3D model to properly account for their electromagnetic properties. The development of such a tool would constitute a valuable contribution for the study of natural photonic structures.

Acknowledgements

The authors gratefully acknowledge partial support from Consejo Nacional de Investigaciones Científicas y Técnicas (CONICET PIP 112-200801-01880) and Universidad de Buenos Aires (UBA-20020100100533).

References

[1] Veselago VG 1968 *The electrodynamics of substances with simultaneously negative values of ε and μ, Sov. Phys. Uspekhi* **10** 509-514

[2] Pendry J B 2000 *Negative refraction makes a perfect lens, Phys. Rev. Lett.*, **85** 18 3966-3969

[3] Tsukerman I 2008 *Negative refraction and the minimum lattice cell size, J. Opt. Soc. Am. B* **25** 927-936

[4] L Jensen , Z Lei , Chan C T and Sheng P 2003 *Photonic Band Gap from a Stack of Positive and Negative Index Materials, Phys. Rev. Lett.* **90** 083901

[5] Grbic A and Eleftheriades G V 2004 *Overcoming the Diffraction Limit with a Planar Left-Handed Transmission-Line Lens, Phys. Rev. Lett.* **92** 117403

[6] Ergin T, Stenger N, Brenner P, Pendry J B and Wegener M 2010 *Three-Dimensional Invisibility Cloak at Optical Wavelengths, Science* **328** (5976) 337-339

[7] Settle M, Engelen R, Salib M, Michaeli A, Kuipers L, and Krauss T F 2007 *Flatband slow light in photonic crystals featuring spatial pulse compression and terahertz bandwidth, Opt. Exp.* **15** (1) 219-226

[8] O'Brien D, Gomez-Iglesias A, Settle M D, Michaeli A, Salib M, and Krauss T F 2007 *Tunable optical delay using photonic crystal heterostructure nanocavities, Phys. Rev. B* **76** (11) 115110

[9] Valentine J,Li J,Zentgraf T,Bartal G,Zhang X 2009 *An optical cloak made of dielectrics, Nat. Mater.* **8** 568

[10] Joannopoulos J, Meade R, Winn J 1995 *Photonic Crystals*, Princeton University Press, United Kingdom.

[11] Moroz A 1999 *Three-dimensional complete photonic-band-gap structures in the visible, Phys. Rev. Lett.* **83** 5274-5277

[12] Russell P 2003 *Photonic crystal fibers, Science* **299** 358-362

[13] Huntington S, Katsifolis J, Gibson B, Canning J, Lyytikainen K, Zagari J, Cahill L, Love J 2003 *Retaining and characterising nanostructure within tapered air-silica structured optical fibers, Opt. Exp.* **11** (2) 98-104

[14] Martelli C, Canning J, Gibson B, Huntington S 2007 *Bend loss in structured optical fibres, Opt. Exp.* **15** (26) 17639-17644

[15] Vukusic P and Sambles J R 2003 *Photonic structures in biology, Nature* **424** 852855

[16] Kinoshita S 2008 *Structural colors in the realm of nature,* World Scientific Publishing Co., Singapore

[17] Berthier S 2007 *Iridescences, the physical colours of insects,* Springer Science + Business Media, LLC, France

[18] Inchaussandague M, Skigin D, Carmaran C and Rosenfeldt S 2010 *Structural color in Myxomycetes, Opt. Exp* **18** 16055-16063

[19] Luna A E, Skigin D C, Inchaussandague M and Roig Alsina A 2010 *Structural color in beetles of South America,* SPIE Optical Engineering + Applications, "The Nature of Light: Light in Nature III", Proc. SPIE Vol. 7782, 778205 (8 pages)

[20] Andrewartha J R, Fox J R and Wilson I J 1977, *Resonance anomalies in the lamellar grating, Optica Acta* **26** 69-89.

[21] Skigin D C and Depine R A 1997, *The multilayer modal method for electromagnetic scattering from surfaces with several arbitrarily shaped grooves, J. Mod. Opt.* **44** 1023-1036

[22] Depine R A and Skigin D C 1998 *Multilayer modal method for diffraction from dielectric inhomogeneous apertures, J. Opt. Soc. Am. A* **15** 675-683

[23] Skigin D C and Depine R A 1998, *Modal method for scattering by arbitrarily shaped multivalued surfaces, J. Mod. Opt.* **45** 1821-1843

[24] Depine R A and Skigin D C 1998 *Modal theory for diffraction from a dielectric aperture with arbitrarily shaped corrugations, Opt. Commun.* **149** (1-3) 117-126

[25] Chandezon J, Dupuis M, Cornet G, Maystre D 1982 *Multicoated gratings: a differential formalism applicable in the entire optical region, J. Opt. Soc. Am.* **72** 839-846

[26] Depine R A and Inchaussandague M E 1994 *Corrugated diffraction gratings in uniaxial crystals, J. Opt. Soc. Am. A* **11** 173-180

[27] Maradudin A A, Michel T R, McGurn A R and Méndez E R 1990 *Enhanced backscattering of light from a random grating, Ann. Phys.* **203** (2) 255-307

[28] Lester M, Skigin D C, Depine R A 2009 *Blaze produced by a dual-period array of subwavelength cylinders, J. Opt. A: Pure Appl. Opt.* **11** 045705

[29] Schmidt G, Kleemann B H 2011 *Integral equation methods from grating theory to photonics: an overview and new approaches for conical diffraction, J. Mod. Opt.* **58** (5-6) 407-423

[30] Taflove A and Hagness S C 2005 *Computational Electrodynamics: The Finite-Difference Time-Domain Method, 3rd ed.,* Artech House Publishers

[31] Yee K 1966 *Numerical solution of initial boundary value problems involving Maxwell's equations in isotropic media, IEEE T Antenn Propag* **14** (3) 302-307

[32] Su MF, El-Kady I, Bader DA, Lin S 2004 *A novel FDTD application featuring OpenMP-MPI hybrid parallelization,* in: Proc. 33rd Int. Conf. Parallel Processing (ICPP), Montreal CA, pp. 373-379

[33] Dolinko A E 2009 *From Newton's second law to Huygens's principle: visualizing waves in a large array of masses joined by springs, Eur J Phys* **30** 1217-1228

[34] Pei T-H and Huang Y-T 2012 *Effective refractive index of the photonic crystal deduced from the oscillation model of the membrane, J Opt Soc Am B* **29** (9) 2334-2338

[35] Shannon C E 1949 *Communication in the presence of noise, Proc Institute of Radio Engineers* **37** (1) 10-21

[36] Courant R, Friedrichs K and Lewy H 1928 *Über die partiellen Differenzengleichungen der mathematischen Physik, Mathematische Annalen* **100** 32-74

[37] Oskooi A F, Roundy D, Ibanescu M, Bermel P, Joannopoulos J D and Johnson S G 2010 *MEEP: a flexible free-software package for electromagnetic simulations by the FDTD method, Comput. Phys. Commun.* **181**, 687-702.

[38] Kolle M 2011 *Photonic structures inspired by nature,* ed Springer-Verlag, Berlin Heidelberg

[39] Cobelli P J, Maurel A, Pagneux V and Petitjeans P 2009 *Global measurement of water waves by Fourier transform profilometry, Exp Fluids* **46** (6) 1037-1047

[40] Higdon R L, 1987 *Numerical absorbing boundary conditions for the wave equation, Math Comp* **179** (49) 65-90

[41] Berenger J 1994 *A perfectly matched layer for the absorption of electromagnetic waves, J Comp Phys* **114** (2) 185-200

[42] Jackson J D 1998 *Classical Electrodynamics 3rd Edition,* ed John Wiley & Sons, Inc., New York, USA

[43] Dolinko A, Skigin D, Inchaussandague M and Carmaran C 2012 *Photonic simulation method applied to the study of structural color in Myxomycetes, Opt. Exp* **20** 15139-15148